NONLINEAR OPTICS

Tailored semiconductors for high-harmonic optoelectronics

Murat Sivis,[1,2]*† Marco Taucer,[1]† Giulio Vampa,[1] Kyle Johnston,[1] André Staudte,[1] Andrei Yu. Naumov,[1] D. M. Villeneuve,[1] Claus Ropers,[2] P. B. Corkum[1]

The advent of high-harmonic generation in gases 30 years ago set the foundation for attosecond science and facilitated ultrafast spectroscopy in atoms, molecules, and solids. We explore high-harmonic generation in the solid state by means of nanostructured and ion-implanted semiconductors. We use wavelength-selective microscopic imaging to map enhanced harmonic emission and show that the generation medium and the driving field can be locally tailored in solids by modifying the chemical composition and morphology. This enables the control of high-harmonic technology within precisely engineered solid targets. We demonstrate customized high-harmonic wave fields with wavelengths down to 225 nanometers (ninth-harmonic order of 2-micrometer laser pulses) and present an integrated Fresnel zone plate target in silicon, which leads to diffraction-limited self-focusing of the generated harmonics down to 1-micrometer spot sizes.

High harmonics generated in gases (*1*, *2*) have been used to study electron and ion dynamics on attosecond time scales (*3*), providing microscopic insights into atomic and molecular systems (*4*, *5*). Recently, a range of solid-state systems have also produced high harmonics of visible (*6*), mid-infrared (*7*, *8*), and terahertz (*9*) driving frequencies. Analogous to the atomic three-step model (*1*), in solids, electron-hole pairs are generated and steered by a strong optical field, causing the emission of higher-energy photons as a result of Bloch oscillations (*6*, *7*, *9*) or recollisions (*8*). Beyond the direct ramifications for all-optical solid-state attosecond spectroscopy (*6*, *8*, *10*, *11*), solid targets offer unique possibilities to control high-harmonic generation by chemical and structural engineering. Specifically, solid-state high-harmonic generation is compatible with established strategies to tailor the electronic structure and optical density of states of materials, using, for example, modulation doping or alloy design in heterostructures (*12*), as well as nanostructures, photonic crystals, and optical metamaterials (*13*).

The utility of high-harmonic generation from engineered targets is twofold: first, as a means to actively manipulate the generation process, and second, as an analytical tool to study the properties of a given heterogeneous system. Thus, combined with the sensitivity to local fields (*8*), harmonics emitted from heterogeneous systems offer singular opportunities that, to date, have been largely unexplored.

We used nanostructured zinc oxide (ZnO) and silicon (Si) samples to confine the driving field leading to enhanced harmonic emission (Fig. 1, A and B). We also locally changed the composition of silicon by ion implantation to alter the electronic structure of the target (Fig. 1, A and C). These two distinct approaches (tailoring structure or composition) provide the basis for a new generation of high-harmonic devices in the solid state, bridging attosecond physics with optoelectronics and photonics. Devices like the structured targets demonstrated in this study will allow great flexibility for designed high-harmonic wave fields.

Intense infrared laser pulses (70-fs pulse duration, 2- to 2.3-μm central wavelength, and 10-kHz repetition rate) focused onto structured targets produce high-order harmonics that can be imaged or detected spectroscopically, as depicted in Fig. 1D. Incident peak intensities exceed 1 TW cm^{-2} at the target [60-μm focal spot size, full width at half maximum (FWHM)], without inducing damage to the structures. The geometry of the grating patterns on the ZnO (Fig. 1B and "target" in Fig. 1D; see the methods section for fabrication details) leads to locally amplified fields by total internal reflection on the cone walls and therefore causes enhanced harmonic emission in "hotspots" (indicated in Fig. 1A). The harmonics are either recorded in the far field behind the target (Fig. 1D and movie S1) or refocused with an objective onto a charge-coupled device (CCD) camera for spatial mapping ("image" in Fig. 1D). The far-field diffraction pattern demonstrates the spatial coherence of the emitted third (red) and fifth (blue) harmonics.

Shown in Fig. 2, A and B, are the diffraction angle–resolved and –integrated harmonic spectra, respectively, from a ZnO grating composed of parallel wedges (Fig. 2C). We observed up to the ninth harmonic order of the fundamental frequency (red and blue curves are measured with different spectrometers; for details, see the methods). The fanlike structure of emitted harmonics reflects the wavelength-dependent diffraction angle. The diffuse scattering signal around 390 nm (figs. S2 to S4) stems from incoherent photoluminescence near the ZnO direct band gap (3.37 eV at room temperature) (*14*).

Figure 2D is an image of the fifth harmonic emitted from the grating in Fig. 2C, illustrating localization and enhancement of the signal (compare the bulk image in Fig. 2E and movies S2 and S3). Similar imaging results for silicon structures are presented in fig. S5. The most prominent feature in Fig. 2D is the enhanced emission along the grating apices. The emission is confined to ~500 nm perpendicular to the wedges, which agrees with field enhancement simulations for this geometry (Fig. 3A). Variations along the bright emission features likely stem from an inhomogeneous chemical composition, as discussed below. Additionally, we observed fringes in and around the structures (Fig. 2D and fig. S5), stemming from interfering harmonics and interference between incident and reflected laser fields.

Figure 2F shows the intensity scaling of the fifth-harmonic signal (normalized to emission area) from the structure in comparison with that from the unstructured bulk crystal. For the structure, on the basis of the imaged hotspot sizes, we estimate an emission area that is reduced by a factor of 25. The emission per area from the structure is much stronger than from the bulk. Comparing the incident intensity required to produce a given signal suggests that the intensity of the driving laser is enhanced by at least one order of magnitude at the hotspot (arrow in Fig. 2F).

For the bulk signal, a transition from fifth- to third-order power scaling [perturbative to nonperturbative (*7*)] with increasing laser intensity is observed. The absence of this transition and the solely nonperturbative intensity scaling of the harmonic emission from the structure confirm the nonperturbative nature of the generation process, as well as the previously determined intensity enhancement. This is consistent with an intensity enhancement of up to 16-fold in our simulation, as shown in Fig. 3A.

Figure 3B plots the normalized fifth-harmonic signals from a bulk region (red) and from the wedge structure (blue) versus the incident laser polarization ellipticity ε, as indicated with the red arrows. The bulk signal steeply decreases with increasing ellipticity and drops to the noise level when ε equals unity, as expected for circular polarization (*7*, *15*). The signal from the structures, however, shows a much weaker ellipticity dependence with substantial emission even at incident circular polarization, indicating an effective birefringence of the structures. The vertical dashed line at ε = 0.6 (corresponding to a 0.2π phase shift between the *p*- and *s*-field components; see the methods) indicates the ellipticity at which the normalized bulk signal equals the signal from the structure at circular polarization (horizontal dashed line). This is consistent with a simulated birefringent phase shift of 0.17π in the hotspot (Fig. 3A), which arises from polarization-dependent total internal reflections during propagation in the structure (*16*). Additionally, both in the experiment and the simulation, we observed different high-harmonic

[1]Joint Attosecond Science Laboratory, National Research Council of Canada and University of Ottawa, 100 Sussex Drive, Ottawa, Ontario K1A 0R6, Canada. [2]4th Physical Institute–Solids and Nanostructures, University of Göttingen, Göttingen, Germany.
*Corresponding author. Email: msivis@uni-goettingen.de
†These authors contributed equally to this work.

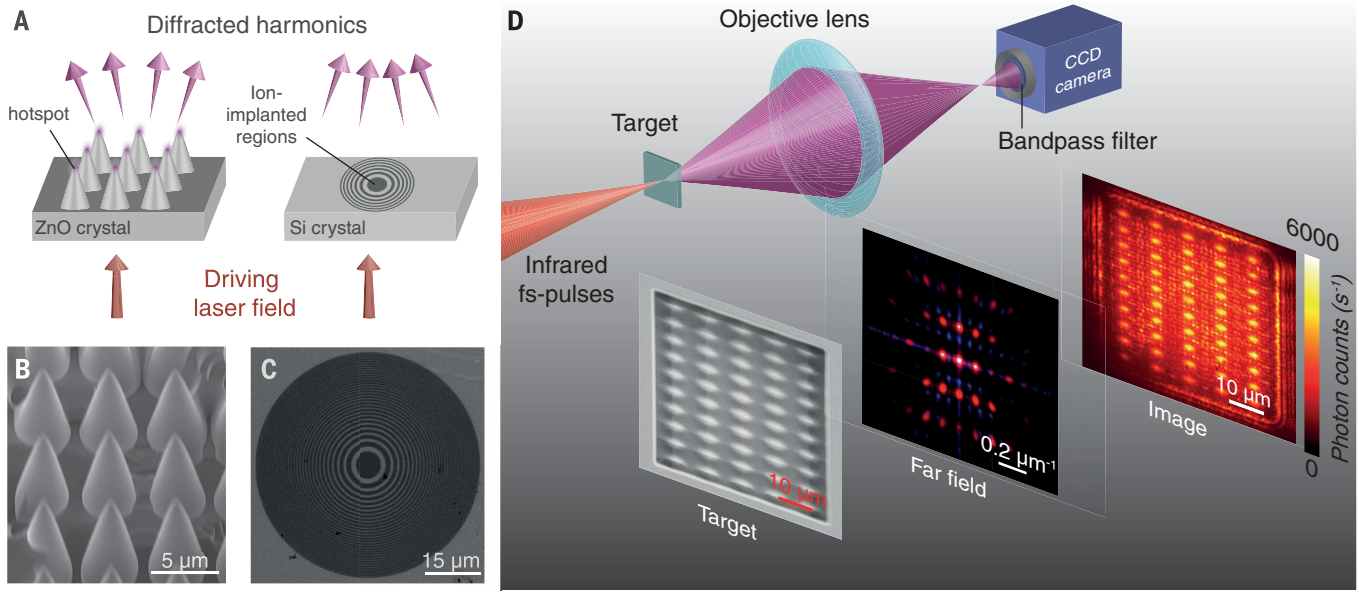

Fig. 1. High-harmonic generation and imaging. (**A**) Illustration of nanostructured (left) and ion-implanted (right) semiconductors. (**B** and **C**) Scanning electron microscope (SEM) images of protruding ZnO cone structures (30°-tilted view) (B) and an ion-implanted Fresnel zone plate (FZP) pattern (darker areas) in silicon (C). (**D**) Schematic of the experimental setup. Infrared illumination of structured ZnO ("target") results in diffracted high-harmonic emission ("far field," recorded 5 mm behind the sample with a three-color complementary metal-oxide semiconductor sensor). The photoluminescence background is subtracted (fig. S2). Bandpass-filtered images of the harmonic distribution ("image") are recorded using a high-magnification objective (numerical aperture, 0.75) and a CCD camera.

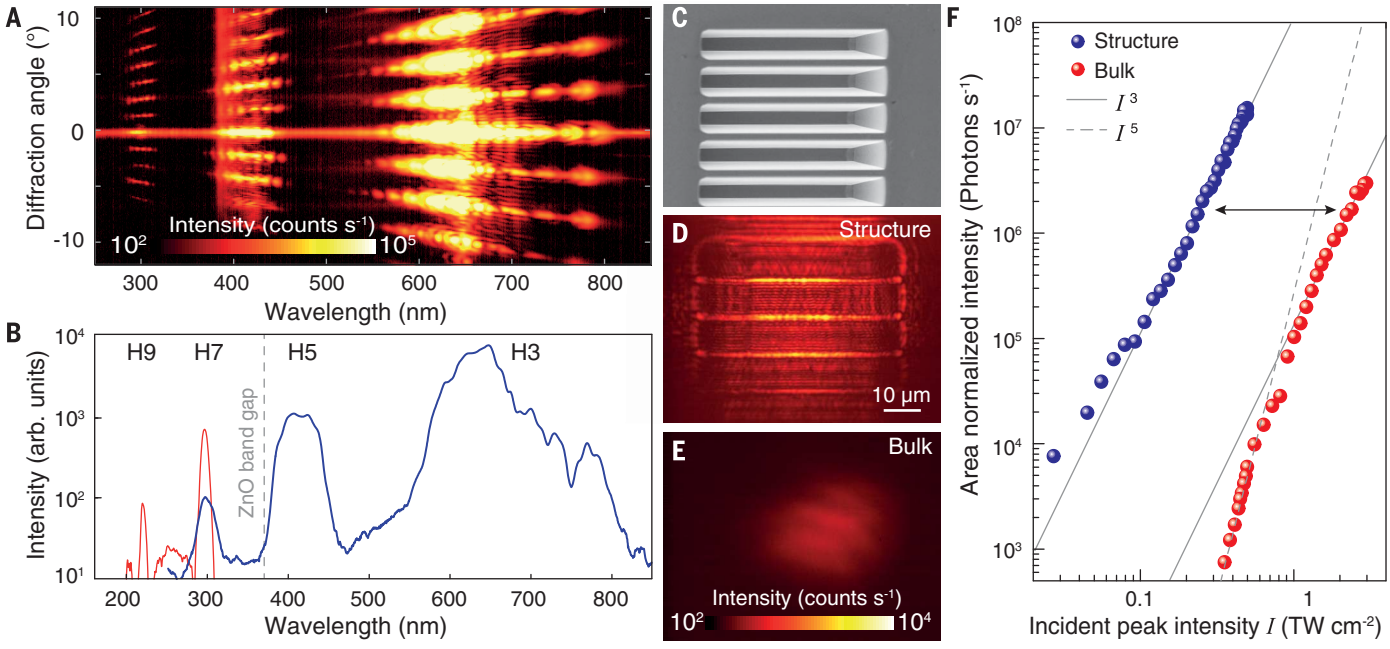

Fig. 2. High-harmonic generation from ZnO structures. (**A** and **B**) Diffraction angle–resolved (A) and diffraction angle–integrated (B) harmonic spectra [harmonic orders are indicated as H3 to H9 in (B)] from the grating structure, using 2.05-μm excitation. arb., arbitrary. (**C**) SEM image of a wedge grating (30°-tilted view). (**D** and **E**) CCD images of 450-nm bandpass–filtered radiation from the structure (D) and bare bulk (E), using 2.25-μm excitation. The scale bar in (D) applies to (C) and (E). (**F**) Intensity scaling of the fifth-harmonic signal from the structure (blue) and the bulk (red), normalized to the area of emission. Dashed (solid) lines indicate perturbative (nonperturbative) scaling. The ordinates in (B) and (F) and all color scales are logarithmic.

yields for *p*- and *s*-polarizations, which stem from a polarization anisotropy of the intensity enhancement α (the solid black curve shows the calculated α^3, considering the cubic intensity scaling).

Beyond surface structuring, chemical modifications allow for tailored high-harmonic generation without changing the targets' morphology. We now demonstrate an integrated, self-focusing harmonic generation source in silicon based on a gallium-implanted Fresnel zone plate (FZP) pattern (inset in Fig. 4A; see the methods section for fabrication details). The FZP has an outer

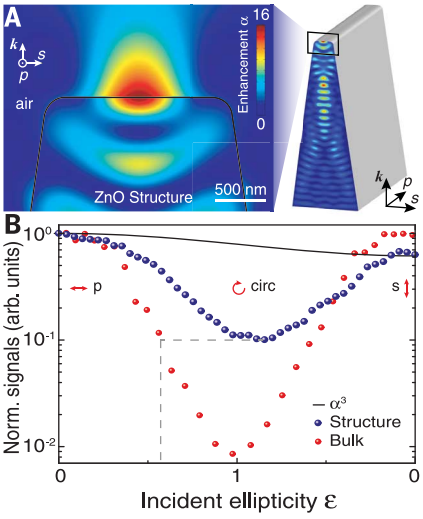

Fig. 3. Field simulation and experimental polarization dependence. (**A**) Simulated intensity distribution in a single wedge structure (cross section perpendicular to the grating grooves; see the schematic on the right) for circularly polarized plane-wave excitation incident along the wave vector **k**. (**B**) Normalized fifth-harmonic signals from the bulk (red) and structure (blue) as a function of incident polarization ellipticity (circ, circularly polarized; p, *p*-polarized; s, *s*-polarized).

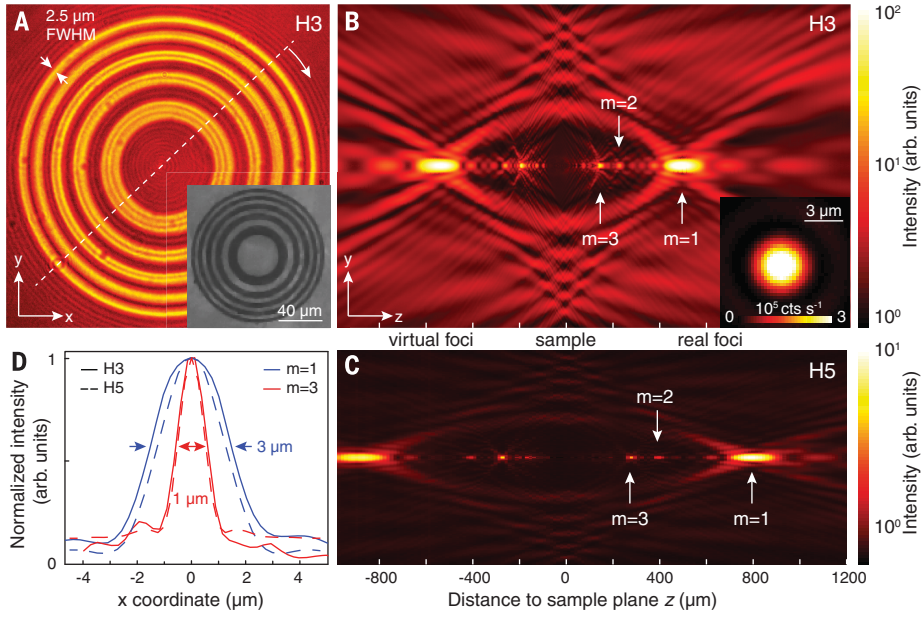

Fig. 4. FZP-pattern high-harmonic generation source. (**A**) Third-harmonic (H3) emission pattern recorded at the sample plane (z = 0 μm). The inset is a SEM image of a gallium-implanted FZP pattern (darker regions) in silicon. (**B** and **C**) Focus scans for the third (H3) (B) and fifth (H5) (C) harmonic. The y axis scales are linked to (A) [the y axis in (C) is reduced by a factor of 1.5]. The focus orders are indicated with m = 1, 2, and 3. The inset in (B) shows the third-harmonic main focus intensity. cts, counts. (**D**) Focus intensity line outs.

diameter of 118 μm and consists of 10 zones. Figure 4A shows an image of the third-harmonic signal from the FZP, with enhanced emission from gallium-implanted regions. The observed spectra contain frequencies up to the ninth harmonic from such structures (fig. S6).

We recorded focus scans of the harmonic intensity distribution by moving the objective relative to the sample plane along the propagation direction (z axis). Shown in Fig. 4, B and C, are the azimuthally integrated third- and fifth-harmonic signals (see the dashed line in Fig. 4A), respectively, revealing the virtual and real foci of the FZP. The focal widths (see the line outs in Fig. 4D) agree with diffraction-limited focusing of the third (fifth) harmonic by using a FZP with a numerical aperture of 0.11 (0.07). We estimate a total of 10^{10} third-harmonic photons per second in the main focus (m = 1; the measured intensity distribution is shown in the inset in Fig. 4B) by taking the transmittance of the optical elements and the CCD quantum efficiency into account. In comparison, the fifth-harmonic photon flux is reduced by a factor of 4. These photon fluxes correspond to peak intensities in the range of 10^8 W cm^{-2}, considering the 70-fs pulse duration.

Additional information about the relative phase of the emission from gallium-implanted and unmodified silicon is contained in Fig. 4, B and C. To estimate the phase difference, we simulated the forward wave propagation (with a Fresnel propagator in the paraxial approximation; fig. S7), starting with the integrated intensity distribution of the FZP at z = 0 μm (Fig. 4, B and C). By variation of the relative harmonic emission phase in the modified and unmodified zones, the error between simulated and measured intensities was minimized for phase differences of π and π/3 for the third and fifth harmonics, respectively.

Whereas the origin of the enhancement in structured semiconductors is evident—the intensity enhancement of the driving field leads to an increased harmonic yield—the mechanism for the enhancement induced by ion implantation warrants further exploration. The implanted gallium ions can act as electron acceptors, adding a positive charge density to the valence band. Furthermore, the implantation process itself causes several types of defects (e.g., vacancies and interstitials), which can likewise alter the generation process by adding states within the band gap (*17*). The observed phase difference between harmonics emitted from modified and unmodified silicon may reflect a charge carrier–induced change in the near-surface refractive index. Alternatively, the phase shift could be due to a change in the dominant generation mechanism—i.e., from inter- to intraband. Regardless of the underlying mechanisms, our findings have important ramifications for the ultrafast sciences in condensed matter and for technological advances in photonics and optoelectronics.

Higher harmonics at extreme-ultraviolet wavelengths, as generated in dielectrics (*6*), would enable spatial resolution below 20 nm by using lensless imaging techniques (*18*) and facilitate all-optical means to study ultrafast structural and electronic dynamics in nanoscopic volumes. As a proof of principle, we reconstructed an emission pattern (fig. S8) by applying a phase-retrieval algorithm to the fifth-harmonic far-field diffraction signal shown in Fig. 1D. Together with spectroscopic capabilities (*6*, *8*, *10*, *11*) and a sensitivity to internal fields (*8*), high-harmonic radiation will contribute to comprehensive insight into active semiconductor devices, such as integrated circuits, promoting novel means to support the development of next-generation devices for information technology. More generally, tailored semiconductors, in combination with plasmonic nanostructures (*19*–*21*), will offer a wealth of applications and fundamental insights in strong-field solid-state physics.

As key aspects of these developments, we have shown that high-harmonic generation in solids is amenable to the extensive technologies of electronics and nanoengineering, with possibilities for manipulating the spatial distribution, intensity, and phase of high-harmonic emission. These results bridge the gap with silicon photonics, promising active control of high-harmonic generation in solids with the potential to create, for example, orbital angular momentum states of extreme-ultraviolet light (*22*). The FZP target is a forerunner of future integrated optical devices and illustrates that the approaches presented here are essential building blocks for a new branch of optoelectronics, which may lead to the development of compact, electrically gateable solid-state emitters for tailored attosecond, extreme-ultraviolet pulses.

REFERENCES AND NOTES

1. P. B. Corkum, *Phys. Rev. Lett.* **71**, 1994–1997 (1993).
2. A. L'Huillier, P. Balcou, *Phys. Rev. Lett.* **70**, 774–777 (1993).
3. P. B. Corkum, F. Krausz, *Nat. Phys.* **3**, 381–387 (2007).
4. J. Itatani *et al.*, *Nature* **432**, 867–871 (2004).

5. H. J. Wörner, J. B. Bertrand, D. V. Kartashov, P. B. Corkum, D. M. Villeneuve, *Nature* **466**, 604–607 (2010).
6. T. T. Luu *et al*., *Nature* **521**, 498–502 (2015).
7. S. Ghimire *et al*., *Nat. Phys.* **7**, 138–141 (2011).
8. G. Vampa *et al*., *Nature* **522**, 462–464 (2015).
9. O. Schubert *et al*., *Nat. Photonics* **8**, 119–123 (2014).
10. G. Vampa *et al*., *Phys. Rev. Lett.* **115**, 193603 (2015).
11. S. Y. You, D. A. Reis, S. Ghimire, *Nat. Phys.* **13**, 345–349 (2016).
12. G. Bastard, *Wave Mechanics Applied to Semiconductor Heterostructures* (Les Editions de Physique, 1990).
13. J. A. Schuller *et al*., *Nat. Mater.* **9**, 193–204 (2010).
14. C. Klingshirn, *Phys. Status Solidi B Basic Res.* **71**, 547–556 (1975).
15. C. Liu, Y. Zheng, Z. Zeng, R. Li, *Phys. Rev. A* **93**, 043806 (2016).
16. R. M. A. Azzam, *JOSA A* **21**, 1559–1563 (2004).
17. E. Rimini, *Ion Implantation: Basics to Device Fabrication* (Springer Science, 1995).
18. S. Zayko *et al*., *Opt. Express* **23**, 19911–19921 (2015).
19. M. Sivis, M. Duwe, B. Abel, C. Ropers, *Nat. Phys.* **9**, 304–309 (2013).
20. S. Han *et al*., *Nat. Commun.* **7**, 13105 (2016).
21. G. Vampa *et al*., *Nat. Phys.* 10.1038/nphys4087 (2017).
22. X. Cai *et al*., *Science* **338**, 363–366 (2012).

ACKNOWLEDGMENTS

We thank D. Crane and B. Avery for technical support and S. Zayko and N. Rubiano da Silva for valuable discussions. The work of the German authors was supported by the Deutsche Forschungsgemeinschaft (DFG) within DFG-SFB755, "Nanoscale Photonic Imaging" (project C08). The Canadian authors gratefully acknowledge financial support from the National Research Council of Canada, the Natural Sciences and Engineering Research Council of Canada, and the Canada Foundation for Innovation/Ontario Research Fund; the U.S. Air Force Office of Scientific Research (AFOSR) under award number FA9550-16-1-0109; and the AFOSR Multidisciplinary University Research Initiative under grant number FA9550-15-1-0037. M.S. and M.T. conducted the experiments with contributions from G.V. and K.J., analyzed the data, and wrote the manuscript with contributions from all authors. M.S. conceived and prepared the nanostructures and carried out the simulations. P.B.C. and C.R. directed the study. All authors discussed the results and interpretation.

SUPPLEMENTARY MATERIALS

www.sciencemag.org/content/357/6348/303/suppl/DC1
Materials and Methods
Supplementary Text
Figs. S1 to S8
References (*23*–*27*)
Movies S1 to S3

15 March 2017; accepted 12 June 2017
10.1126/science.aan2395

Tailored semiconductors for high-harmonic optoelectronics

Murat Sivis, Marco Taucer, Giulio Vampa, Kyle Johnston, André Staudte, Andrei Yu. Naumov, D. M. Villeneuve, Claus Ropers and P. B. Corkum

Science **357** (6348), 303-306.
DOI: 10.1126/science.aan2395

Hitting the highs in solid state

The ability to generate high harmonics of optical frequencies through the nonlinear interaction between intense light pulses and gas atoms has opened up the area of ultrafast optics and spectroscopy. Sivis *et al.* now show that high harmonics can also be generated with a solid-state sample. They used nanofabricated structured targets of ZnO and varied the chemical composition of the sample to demonstrate that (modest) high harmonics can be generated as the light interacts with the target materials. The results present the possibility of developing solid-state ultrafast optical devices.

Science, this issue p. 303